1999

Analysis of Ductile to Cleavage Transition in Part-Through Cracks Using the Cell Model Incorporating Statistics

Xiaosheng Gao
University of Akron, main campus, xgao@uakron.edu

J. Faleskog

C. Fong Shih

Analysis of ductile to cleavage transition in part-through cracks using a cell model incorporating statistics

X. GAO[1], J. FALESKOG[2] and C. FONG SHIH[3]

Division of Engineering, Brown University, Providence, RI 02912, USA, [1]Presently at Department of Civil Engineering, University of Illinois, Urbana, IL 61801, USA, [2]Presently at Department of Solid Mechanics, Royal Institute of Technology, S-100 44 Stockholm, Sweden, [3]Presently at Institute of Materials Research and Engineering, National University of Singapore, 10 Kent Ridge Crescent, Singapore 119260

Received in final form 22 November 1998

ABSTRACT This paper describes an approach to study ductile/cleavage transition in ferritic steels using the methodology of a cell model for ductile tearing incorporating weakest link statistics. The model takes into account the constraint effects and puts no restriction on the extent of plastic deformation or amount of ductile tearing preceding cleavage failure. The parameters associated with the statistical model are calibrated using experimental cleavage fracture toughness data, and the effect of threshold stress on predicted cleavage fracture probability is investigated. The issue of two approaches to compute Weibull stress, the 'history approach' and the 'current approach', is also addressed. The numerical approach is finally applied to surface-cracked thick plates subject to different histories of bending and tension, and a new parameter, ψ, is introduced to predict the location of cleavage initiation.

Keywords ductile tearing, cleavage fracture, constraint effects, cell model, weakest link statistics, finite elements.

INTRODUCTION

The competition between cleavage fracture and ductile tearing determines the macroscopic fracture toughness of ferritic steels in the ductile/brittle transition regime. Ductile crack growth can occur under increasing load and the structure can withstand a significant amount of ductile tearing without substantial loss of load-bearing capacity. Cleavage fracture, on the other hand, leads to catastrophic failure of structure components, and the onset of cleavage is then the critical mechanism limiting the load-bearing capacity of the structure. Moreover, it has been noticed that stable ductile crack growth may eventually give way to cleavage fracture.

A typical steel contains inclusions on two different size scales. The large inclusions, e.g. manganese sulphide, range in size from 1 to 5 microns and have mean spacings of the order of 100 microns. A second and larger population of submicron-sized inclusions, e.g. carbides, are found within grains and at grain boundaries. Voids nucleate from large inclusions at relatively low stress levels. Under increasing strain the voids grow and coalesce forming new crack surfaces, thereby advancing the crack by the ductile tearing mechanism.

The cell model for non-linear fracture, originally proposed by Xia and Shih,[1–3] together with the two-step model-calibration scheme (micromechanics calibration and fracture process calibration) proposed by Faleskog *et al.*[4] and Gao *et al.*,[5] has been successfully applied to predict details of the load, displacement and ductile crack growth in fracture specimen geometries known to give rise to significantly different crack tip constraints and crack growth resistance behaviours, including surface flaws in thick plates subjected to different states of bending and tension.[5–8] The key feature of this model is modelling the material in front of the crack as a layer of similarly sized void-containing cubic cells. Each cell is a three-dimensional material element which is initially a cube with dimension D comparable to the spacing between the large inclusions. Each cube contains a centred spherical void of initial volume fraction f_0. For the most part, the Gurson–Tvergaard relation can be used to describe the stress–strain behaviour of a single void-containing cell element.[9–11] As the cell is strained, the void in the cell grows. Eventually the strain-hardening of the matrix is insufficient to compensate for the reduction in the cell ligament area caused by void growth. Under these conditions, the cell begins to lose

stress-carrying capacity. Shortly after, microvoids nucleate from secondary inclusions bringing about the final coalescence phase that allows the crack to advance across that cell.

The process of transgranular cleavage fracture has been attributed primarily to slip-induced cracking of carbide particles, generally located on grain boundaries, followed by unstable propagation of the resultant cracks into the surrounding ferrite matrix.[12] Carbide particles which are 'eligible' for cleavage initiation are those: (i) under sufficient tensile stress; (ii) with orientations favorable for nucleating a crack; and (iii) producing high enough energy release rate.[14] Therefore, the initiation of cleavage fracture depends on the probability of finding the 'eligible' particles within the stressed volume. It has been noticed that crack growth by ductile tearing causes a significant increase in constraint ahead of the crack, elevating the stress level and increasing the size of the high stress zone, therefore increasing the probability of cleavage fracture.[3,15] Within the ductile/brittle transition regime, it is often observed that a crack initiates and grows by ductile tearing, but final failure occurs by catastrophic cleavage fracture.[16]

Curry and Knott[17] have shown that carbide-induced cleavage fracture in ferritic steels is of a statistical nature. Treatment of the initiation of unstable cleavage fracture by way of extreme value statistics has been discussed by Beremin,[18] Mudry,[19] Wang,[13] Bakker and Koers,[20] and Wallin[21] among others. In these studies a weakest link mechanism was assumed for cleavage fracture and cleavage probability was described by a Weibull distribution. More recently, Koers *et al.*,[22] Xia and Shih,[3] and Ruggieri and Dodds[15] extended this approach to account for ductile crack growth prior to cleavage fracture. Weibull stress σ_w was adopted as the local parameter to describe crack-tip conditions, and cumulative probability of unstable cleavage fracture was then phrased in terms of a critical value of σ_w which may be attained prior or following some amount of stable ductile crack extension. These studies captured the strong effects of ductile tearing and constraint variation on macroscopic cleavage fracture toughness.

In this paper, following the approach taken by Xia and Shih,[3] we apply the methodology of the cell model incorporating weakest link statistics to study ductile/cleavage transition in fracture specimens of a low-strength, high-hardening pressure vessel steel ($2\frac{1}{4}$ Cr 1 Mo). The model-specific cell parameters (micromechanics parameters q_1, q_2 and f_E, and fracture process parameters D and f_0) have been calibrated and verified in Ref. [5]. The parameters associated with Weibull distribution, the shape factor m and the scaling stress σ_u, are calibrated using the experimental data of Wallin.[21] The effect of threshold stress on the prediction of cleavage probability is discussed, and the difference of using the 'history approach' and the 'current approach' in Weibull stress calculation is also examined. Finally, the model is applied to predict ductile/cleavage transition in surface-cracked thick plates subject to different combinations of bending and tension. It captures the strong effect of constraint on cleavage probability. A new parameter ψ, defined as $(\sigma_w/\sigma_u)^m$ per unit length along the crack front, is introduced, which reaches a maximum at the location where cleavage initiation is most likely to take place.

CELL MODEL FOR DUCTILE TEARING

At the microscale level, ductile extension of a pre-existing macrocrack in common structure and pressure vessel steels proceeds in a multistep mode of material failure which reflects several interacting, simultaneous mechanisms:[23] (i) nucleation of microvoids by fracture/decohesion of larger inclusions; (ii) subsequent growth of the larger microvoids; (iii) localization of plastic flow between the enlarged voids; and (iv) final tearing of ligaments between the enlarged voids, assisted by the rapid nucleation, growth and coalescence of secondary microvoids, to create new surfaces of the macrocrack. Micrographs show these processes of void growth and coalescence are confined to a narrow zone ahead of the crack front having a thickness of no more than a few hundred microns.

The above failure mechanism suggests the use of an aggregate of similarly sized cells which forms the material layer of thickness D to model the ductile failure process. In many materials, void nucleation from large inclusions often occurs at relatively low stress, well below the peak macroscopic stress that develops ahead of the crack front. For the purpose of analysis, the voids can be assumed to be present in the material layer at the very outset, thus this material layer has an initial void volume fraction f_0.[1–3] The cell size, D, provides an explicit material length scale for the computational model which can be extracted from crack growth data.

For the most part, the Gurson–Tvergaard (GT) relation[9–11] is used to describe the growth of a single void in a cell and the associated macroscopic softening. At the heart of the GT model is the yield condition

$$\Phi = \frac{\sigma_e^2}{\bar{\sigma}^2} + 2q_1 f \cosh\left(q_2 \frac{3\sigma_m}{2\bar{\sigma}}\right) - 1 - q_1^2 f^2 = 0 \qquad (1)$$

Here, f is the current void volume fraction, $\bar{\sigma}$ is the current matrix flow strength, σ_e is the macroscopic effective Mises stress, σ_m is the macroscopic mean stress, and q_1 and q_2 are adjustment parameters to improve the model predictions. The most widely used form, which

applies to strain-hardening material under the assumption of isotropic hardening, is adopted here.

The void in a cell grows under increasing strain. Eventually, the strain-hardening of the matrix is insufficient to compensate for the reduction in the cell ligament area caused by void growth with the result that the cell begins to lose stress-carrying capacity. At some void volume fraction, the cell no longer supports any traction across the plane of the crack and the crack advances across that cell. The GT model does not supply the traction relation during the final phase prior to material separation. Therefore, it is necessary to introduce a criterion for final cell rupture and a traction-separation relationship for that event. In studies to date, the GT relation is used until the value of f reaches f_E, at which point all tractions carried by the cell element are eliminated with the aid of a linear force reduction versus cell elongation relationship.

The cell model has to be calibrated specifically for the material before it can be used to predict the fracture behaviour of a structural component. q_1 and q_2 in GT flow potential can be calibrated by studying the hole-growth mechanism taking into account matrix strain-hardening and strength. f_E and cell extinction scheme can be decided from the study of coalescence mechanism. D and f_0 can be calibrated using fracture test data. See Refs [4,5] for details of cell model calibration.

STATISTICAL MODEL FOR CLEAVAGE FRACTURE

Cleavage fracture is assumed following a weakest link mechanism. I.e. at some point during the loading, a microcrack nucleates at a critical second phase inclusion and this event is sufficient to precipitate catastrophic cleavage fracture. Only particles within the plastic zone are considered to be able to cause cleavage initiation as cleavage fracture is always preceded by some amount of plastic deformation. Both two-parameter and three-parameter Weibull models have been employed to describe the cleavage probability.[2,13,15,17–22] In the two-parameter Weibull model, it is assumed that cleavage fracture may occur by the onset of plastic deformation, while in the three-parameter Weibull model a threshold stress is assumed below which cleavage fracture can not be triggered. If the occurrence of plasticity is taken as the lower bound, it would mean that for a temperature far above the brittle to ductile transition regime there is still a probability for cleavage. The three-parameter Weibull model, on the other hand, avoids this unrealistic outcome because a sufficiently high threshold will not allow cleavage fracture at higher temperature.[22] However, there are still debates on using the two-parameter or three-parameter model, and the determination of a physically meaningful value for threshold stress still remains an open issue.

The expression for the cumulative probability of failure by cleavage, P_f, suited for finite element analysis is

$$P_f = 1 - \exp\left[-\left(\frac{\sigma_w}{\sigma_u}\right)^m \right] \tag{2}$$

with the Weibull stress defined by

$$\sigma_w = \left[\sum_{i=1}^{n} (\sigma_1^i - \sigma_{th})^m \frac{V_i}{V_0} \right]^{1/m} \quad \text{for } V_i$$
$$\text{where } \sigma_1^i \geqslant \sigma_{th} \quad \text{and} \quad \bar{\varepsilon} > 0 \tag{3}$$

Here m is a shape factor, σ_{th} is a threshold stress ($\sigma_{th} = 0$ leads to the formulation of the two-parameter Weibull stress), σ_u is a scaling stress (63.2% Weibull stress value) and V_0 is a reference unit volume. V_i is the volume of the ith element and σ_1^i is the maximum principal stress in V_i; n is the total number of material elements meeting the threshold stress and non-zero plastic strain condition stated in equation (3). In this study, σ_1 in equation (3) is taken as the maximum stress that the material point has experienced during the entire loading history in order to assure that cleavage probability increases with increased loading, following the arguments by Bakker and Koers.[20] We also computed Weibull stress using the current maximum principal stress, and examined the difference of these two approaches in Section 4.3.

Note from equations (2) and (3) that σ_u and m can be combined into a single parameter, $\sigma_u^m V_0$, which should be regarded as a material constant. Therefore, the same value of V_0, although it can be an arbitrary constant, must be used in calibrating Weibull parameters, m and σ_u, and computing Weibull stress for different specimens. In this paper, V_0 is fixed at $V_0 = D^3$ for all cases. Parameters m and σ_u may or may not depend on temperature but are considered invariant of crack geometry and loading history.

The Weibull stress incorporates the combined effect of sampling volume and loading intensity. It can be seen from equation (2) that the relation between σ_w and cumulative probability for cleavage fracture P_f depends on a material scaling parameter σ_u and a microstructure parameter m which is associated with the size distribution of carbide particles. For a given material P_f depends on σ_w alone, and the effects of geometry, applied load and ductile crack growth history enter into cleavage prediction through σ_w only. Incorporating the above statistic model with the cell model for ductile tearing, the computational approach is not restricted by the extent of plastic deformation or amount of ductile tearing preceding cleavage failure.

MODEL CALIBRATION

Material

The material dealt with in this study is a low-strength, high-hardening pressure vessel steel ($2\frac{1}{4}$ Cr 1 Mo) taken from a decommissioned chemical reactor. All the experiments were performed at room temperature, which falls in the middle of the brittle to ductile transition interval suggested by the Charpy-V impact test.[24] Young's modulus of the material $E = 206$ GPa, and Poisson's ratio $\nu = 0.3$. The 0.2% offset yield strength at room temperature $\sigma_{ys} = 260$ MPa and ultimate strength $\sigma_{uts} = 530$ MPa. The strain-hardening characteristics of this material at room temperature closely follow those of a simple power-law model with the true stress–strain relation:

$$\begin{aligned} \varepsilon &= \frac{\sigma}{E} && \sigma < \sigma_0 \\ \varepsilon &= \frac{\sigma_0}{E}\left(\frac{\sigma}{\sigma_0}\right)^{1/N} && \sigma \geqslant \sigma_0 \end{aligned} \tag{4}$$

Here σ_0 is the tensile yield stress and N is the strain hardening exponent. The choice of $N = 0.2$ and $\sigma_0 = 210$ MPa yields very good fit to the measured uniaxial tensile response (corrected for necking according to the Bridgeman type of procedure).

Parameters for cell model

The micromechanics calibration for the material in this study has been carried out by Faleskog *et al.*[4] and Gao *et al.*,[5] which suggests the hole-growth parameters to be $q_1 = 2$ and $q_2 = 0.77$. The critical porosity $f_E = 0.2$ and a linear force reduction versus cell elongation relationship for cell extinction were proved to be appropriate.[5] The fracture process calibration has been performed using experimental data from single-edge-notch specimens loaded in three-point bending. The CTOD at ductile fracture initiation was measured to be about 300 microns (cf. Faleskog) [25]—this value was assigned to D. The calibration using a plane strain model and test data from a side-grooved specimen suggested $f_0 = 0.0045$, and the calibration using a full three-dimensional model and test data from a plane-sided specimen suggested a slightly smaller value $f_0 = 0.0035$. A detailed discussion of the above fracture process calibration and verification is given by Gao *et al.*[5]

Wallin[21] reported an extensive set of test data of this material consisting of 105 25-mm-thick CT specimens with side grooves of 20% thickness (10% on each side). The initial crack length to specimen width ratio, a/W, is 0.6, and the specimen width $W = 50$ mm. The experiment was performed at room temperature. Most of the specimens failed by cleavage fracture following some amount of ductile tearing, while seven of them did not cleave after $3.5 \sim 5.5$ mm of ductile crack extension before the test was terminated. Because crack growth in side-grooved specimens is almost uniform through the whole thickness, the plane strain model is employed to simulate Wallin's experiment, which overcomes the difficulties introduced by side-grooves to the finite element modelling.

Because of symmetry, only half of the specimen needs to be modelled. Figure 1(a) displays the finite element mesh. A zone of highly refined rectilinear mesh stretches out on the ligament ahead of the crack tip where the crack growth will occur [Fig. 1(b)]. A row of uniformly sized void-containing cell elements with the dimension of $D/2 \times D/2$ is embedded in the highly refined mesh directly ahead of the initial crack. The body outside the row of cell elements is represented by regular elements. There are 700 elements in the mesh including 56 cell elements.

Figure 2(a) compares the model-predicted fracture resistance curve with the experimental data. The solid line represents the results of our numerical model and the filled circles denote test data from Ref. [21], in which the $\mathcal{J}$-integral values were evaluated at cleavage initiation or test termination, and the amount of ductile crack growth was measured by scanning electron microscopy. The agreement between model prediction and

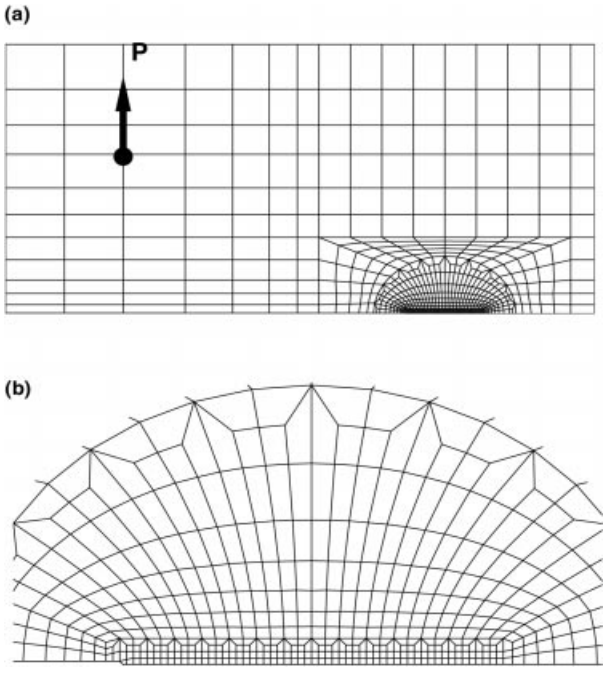

Fig. 1 Finite element model of a 1T CT specimen ($a/W = 0.6$) for plane strain analysis. (a) Half of the specimen. (b) Region near the initial crack tip including cell elements with the dimension of $D/2 \times D/2$.

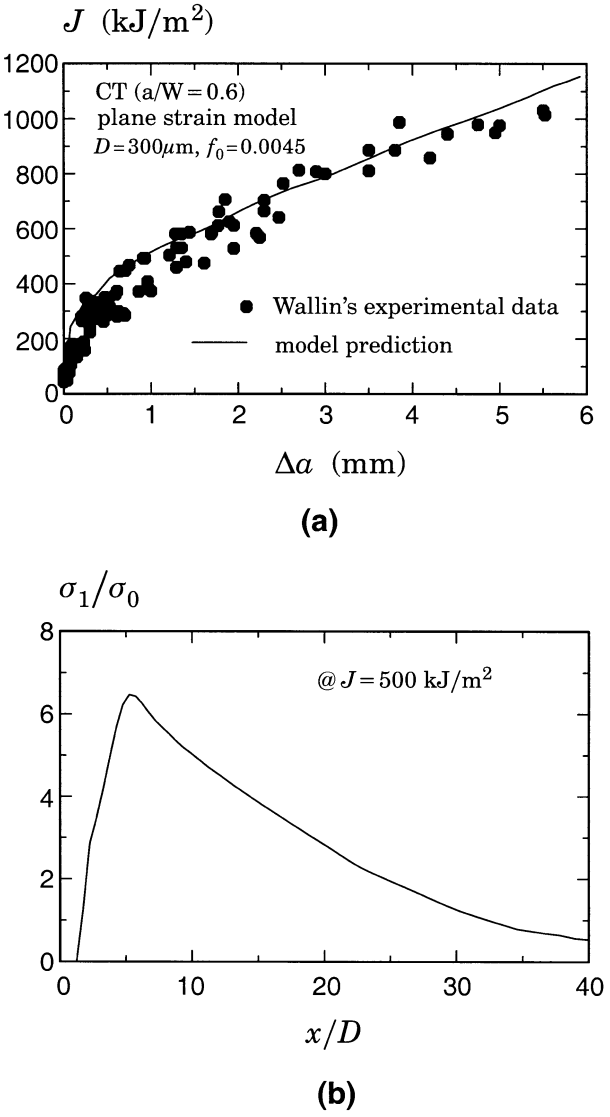

Fig. 2 (a) Comparison of the predicted crack growth resistance curve from the plane strain model with the experimental data for the CT specimen ($a/W = 0.6$, side-grooves of 20% thickness). The symbols represent Wallin's experimental data and the solid line represents the numerical result. (b) The distribution of σ_1 ahead of the crack in the CT specimen at $\mathcal{J} = 500$ kJ/m^2.

experimental data is very good, which verifies the parameters used in our numerical model.

Parameters for Weibull distribution

From equation (2) it is known that $\log\{\log[1/(1-P_f)]\}$ is a linear function of $\log \sigma_w$ with the slope equal to m. Therefore, the Weibull parameters can be determined by the following iterative process for a preassumed value of threshold stress σ_{th}. Assume a trial value for m and compute the Weibull stress at the experimentally observed fracture points from equation (3). Using the least square method (or other methods) to get a linear regression of $\log\{\log[1/(1-P_f)]\}$ versus $\log \sigma_w$, with P_f values at cleavage fracture points taken equal to the rank probability of the cleavage fracture points within the series, $P_{rank} = (i-0.5)/n$, where i denotes the rank number and n denotes the total number of tests. The linear regression results in a slope m^* and a value for σ_u. If $m^* \neq m$, set $m = m^*$ and repeat the above process until m^* and m are equal.

Applying the above procedure to Wallin's experiments, we have calibrated Weibull parameters for different values of threshold stress. In our numerical calculations, the net thickness of the specimen, $0.8B = 20$ mm, has been used in computing Weibull stress, i.e. V_i in equation (3) is equal to $A_i \times 0.8B$, where A_i is area of the ith element in the plane strain model. For $\sigma_{th} = 0$, $2\sigma_0$ and $4\sigma_0$, the calibrated sets of (m, σ_u) are $(11.08, 11.86\sigma_0)$, $(6.50, 12.88\sigma_0)$ and $(1.95, 109.24\sigma_0)$. The value of σ_{th} should be chosen such that the cleavage process zone ($\sigma_1 \geqslant \sigma_{th}$ and $\bar{\varepsilon} > 0$) is large enough to contain a sufficiently large number of grains. Figure 2(b) shows the distribution of σ_1 ahead of the crack at $\mathcal{J} = 500$ kJ/m^2, where the peak value of σ_1 reaches about $6.4\sigma_0$. For $\sigma_{th} = 4\sigma_0$, the length of the cleavage process zone $l \approx 11D$, which is 80 times the grain size (grain size of this material is about 40 μm).[25] The physical length scale is also apparent in fig. 26 of Ref. [25] where iso contours of maximum principal stress are drawn on a micrograph pertaining to the load level at which cleavage failure occurred.

Figure 3(a) displays the variation of m with σ_{th}. As can be seen, a larger σ_{th} leads to a smaller m. Also note that m decreases virtually linearly with the increase of σ_{th}. Figure 3(b) shows that the calibrated scaling stress, σ_u, increases as a larger value of σ_{th} is assumed. The increase of σ_u is more pronounced for $\sigma_{th} > 3\sigma_0$.

Because there is not a trivial way to determine σ_{th}, it is worthwhile to check the sensitivity of the prediction of cleavage probability to the choice of σ_{th}. Figure 4(a) compares the predicted cleavage probabilities for three values of σ_{th}: $\sigma_{th} = 0$, which leads to a two-parameter Weibull model, $\sigma_{th} = 2\sigma_0$ and $\sigma_{th} = 4\sigma_0$.These three curves almost coincide and the effect of σ_{th} is negligible. The symbols in Fig. 4(a) indicate the rank probabilities and the $\mathcal{J}_c$ values at failure. The calibrated statistical model, regardless of the assumed σ_{th} value, fits the experimental data very well.

To further investigate the effect of σ_{th} on cleavage prediction, we consider a side-grooved (20% thickness) 1T-SE(B) specimen with $a/W = 0.1$ and $W = 50$ mm, which has a much lower level of crack tip constraint than the deep-cracked CT specimen ($a/W = 0.6$). Figure 4(b) shows the comparison of the predicted cleavage probabilities for three values of σ_{th}: 0, $2\sigma_0$ and $4\sigma_0$.

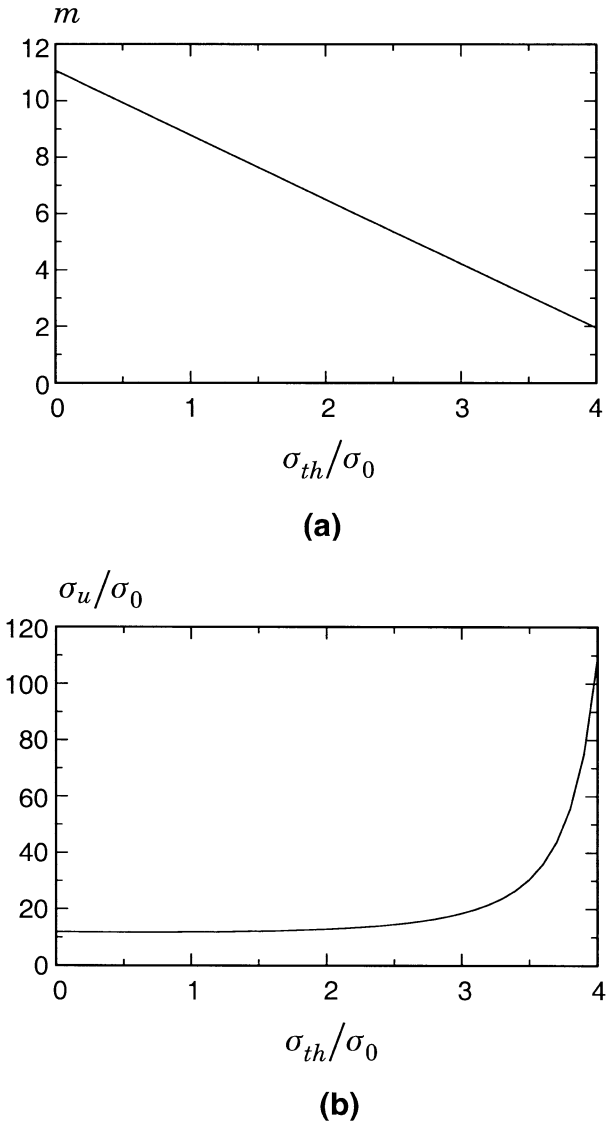

Fig. 3 Calibrated Weibull parameters as functions of threshold stress. (a) m versus σ_{th}, (b) σ_u versus σ_{th}.

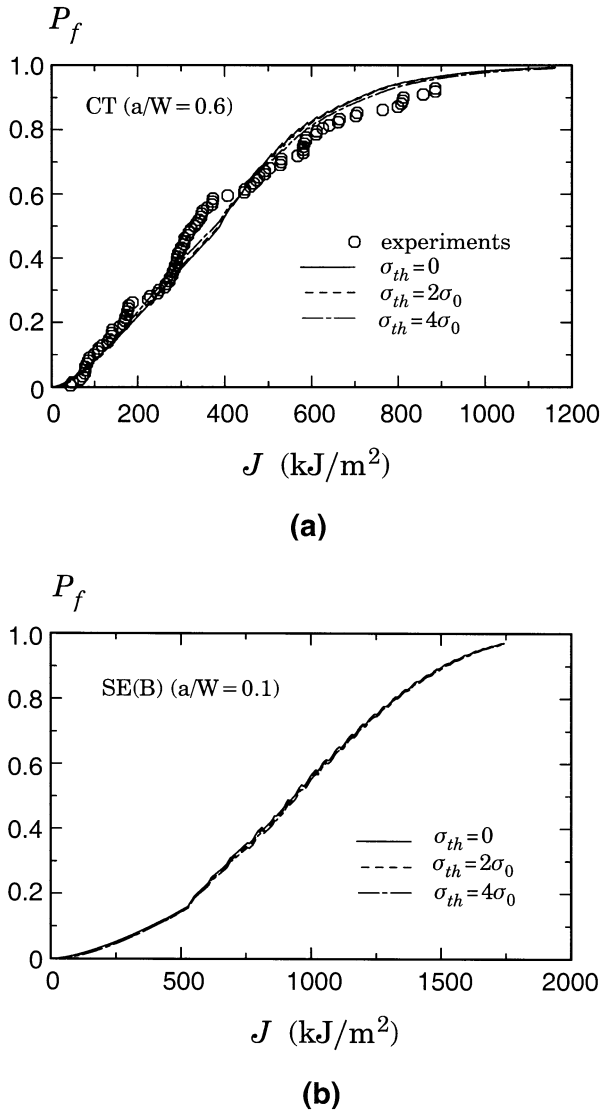

Fig. 4 Effect of σ_{th} on cleavage prediction. The solid line represents the result of $\sigma_{th} = 0$, the dashed line represents the results of $\sigma_{th} = 2\sigma_0$ and the dash–dotted line represents the results of $\sigma_{th} = 4\sigma_0$. (a) CT, $a/W = 0.6$, where the open circles indicate the measured cleavage fracture toughness and the rank probabilities. (b) SE(B), $a/W = 0.1$.

Again, the effect is negligible. I.e. although the subject of using the two-parameter Weibull model or three-parameter Weibull model and finding the realistic value for threshold stress merits further work, the issue is not critical for the material in this study.

Figure 5 compares the evolution of cumulative cleavage probability with the increase of loading ($\mathcal{J}$), and amount of ductile crack growth for the higher constraint, deep-cracked CT specimen and the lower constraint, shallow-cracked SE(B) specimen. The results are based on the threshold stress $\sigma_{th} = 4\sigma_0$. It is clear that the lower constraint specimen has a much higher fracture toughness and can withstand a greater amount of ductile tearing at a certain cumulative cleavage probability. For $P_f = 0.5$, the fracture toughness $\mathcal{J}_c$ is 378 kJ/m^2 for CT specimen and 945 kJ/m^2 for SE(B) specimen; the amount of ductile tearing prior to cleavage is 0.4 mm for CT specimen and 1.4 mm for SE(B) specimen. This figure demonstrates clearly the effect of constraint on the probability of cleavage fracture.

Another issue of the statistical model is whether the current value of maximum principal stress (hereafter referred to as 'current approach') or the maximum principal stress the material point experienced during the loading history (hereafter referred to as 'history

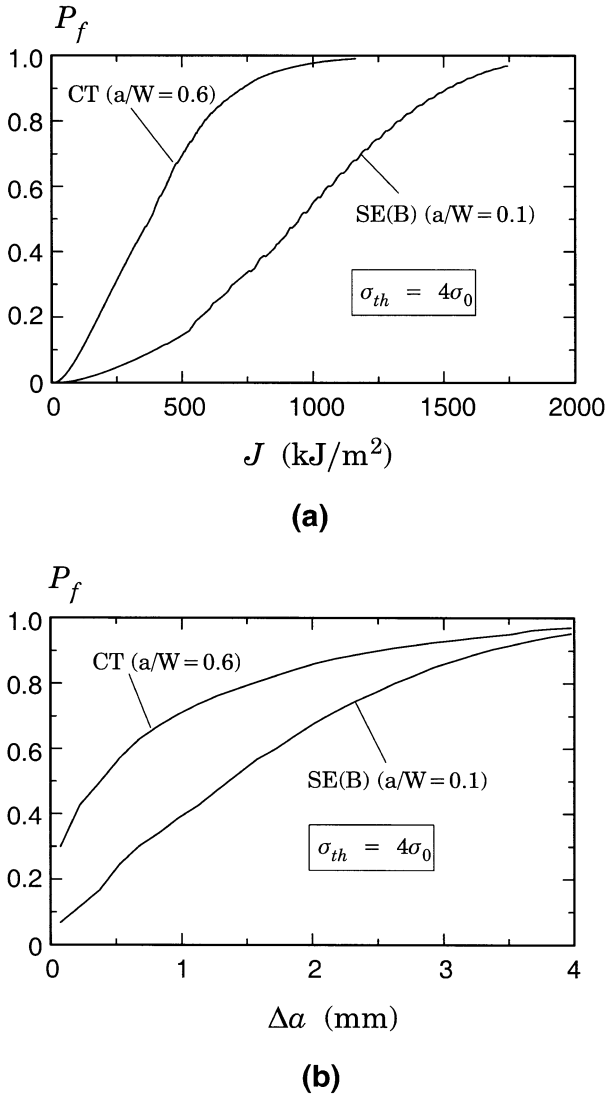

Fig. 5 Comparison of the evolution of cumulative cleavage probability with the increase of $\mathcal{J}$ and amount of ductile crack growth for the deep-cracked CT specimen and the shallow-cracked SE(B) specimen. (a) P_f versus $\mathcal{J}$, (b) P_f versus Δa.

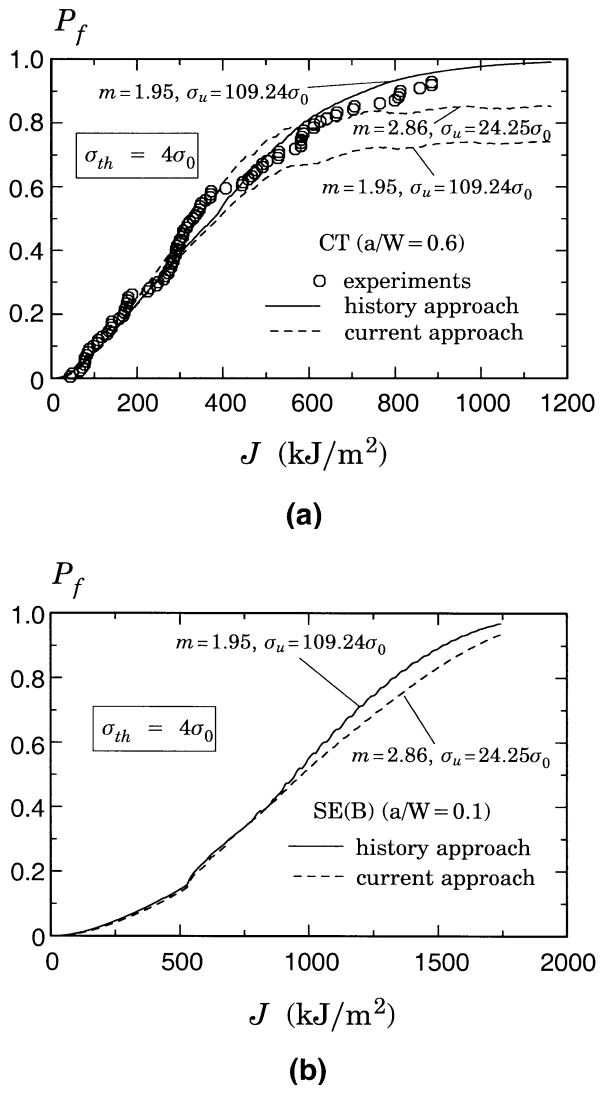

Fig. 6 Comparison of predicted cleavage probability using 'history approach' (solid line) and 'current approach' (dashed line). (a) CT, $a/W = 0.6$, where the open circles indicate the measured cleavage fracture toughness and the rank probabilities. (b) SE(B), $a/W = 0.1$.

approach') should be used in the Weibull stress calculation. In the above calculations, the 'history approach' was employed, and it should be pointed out that only this approach is strictly consistent with weakest link modelling. Figure 6(a) compares the predicted cleavage probabilities using both approaches. For $\sigma_{th} = 4\sigma_0$ and using $m = 1.94$ and $\sigma_u = 109.24\sigma_0$, the difference between predictions from these two approaches remains small until $\mathcal{J}$ reaches 550 kJ/m^2. For $\mathcal{J} > 550$ kJ/m^2, the 'history approach' predicts a continuous increase of cleavage probability as load increases, whereas the 'current approach' saturates at a constant level of failure probability less than unity. If we use the 'current approach' and repeat the above iterative process to determine Weibull parameters, it turns out that for $\sigma_{th} = 4\sigma_0$, the calibrated Weibull parameters are $m = 2.85$ and $\sigma_u = 24.25\sigma_0$. The calculated cleavage probability using these values is also presented in Fig. 6(a). Again, the cleavage probability saturates at a constant level of failure probability less than unity as $\mathcal{J} > 550$ kJ/m^2. It seems that the 'history approach' gives a better fit of the experimental data indicated by open circles. Figure 6(b) compares the results from these two approaches for the shallow-cracked SE(B) specimen. The difference between the two curves is negligible for $\mathcal{J} < 1000$ kJ/m^2. As the applied load continuously increases, the 'history approach' predicts a higher cleavage probability than the 'current approach' does.

APPLICATION TO SURFACE-CRACKED PLATES

Specimen geometry and FEM modelling

Faleskog and co-workers[24,25] conducted a series of tests on surface-cracked thick plates subject to different histories of bending and tension at room temperature. A small amount of ductile crack growth was observed before the specimens were finally fractured by cleavage. For some specimens, crack closure occurred during the tests and those specimens are not analysed here.

Figure 7(a) illustrates the geometry and loading scheme for the tested surface-cracked plate specimens (SCT). The specimen is a slightly curved plate with thickness t_2, overall length $2L$ and width $2H$. The initial semi-elliptical crack in the centre of the plate has a surface length of $2c$ and maximum depth of a. Fatigue sharpening of a machined slit formed the crack. The longitudinal mid-planes of the cracked and uncracked sections have an initial offset, distance e, to induce a secondary bending moment during the loading which opens the crack. The specimen ends are welded to thick, circular plates at a small slant angle, θ_0, with respect to the plane of the plates. These in turn are mounted by screws along their periphery to the servo-hydraulic testing machine (an additional bending moment results from the slant angle θ_0). By varying the offset e and angle θ_0, the test procedure generates different M–N loading histories, where N denotes the membrane load and M the bending moment acting on the crack plane.

Two SCT specimens (SCT-4, 6) were loaded in combined bending and tension as described above, where specimen SCT-6 was subjected to the highest bending load. Specimen SCT-2 was subjected to pure tension and specimen SCT-1 was loaded in three-point-bending. Table 1 summarizes the various dimensions for these specimens, and Fig. 7(b) illustrates the M–N loading histories for these specimens.

Table 1 Geometrical data for SCT test specimens

Specimen no.	L	H	t_1	t_2	c	a	e	θ_0
SCT-1	240	155	50	50	49.2	23.9	0.0	0.0
SCT-2	265	153	50	67	46.35	22.1	0.0	0.0
SCT-4	320	156	50	70	44.92	20.24	2.5	0.00625
SCT-6	319	155	50	70	50.05	22.3	30	0.0135

θ_0 is in radian and all other dimensions are in mm.

Figure 8 shows a typical finite element mesh for a SCT specimen. Symmetry of the geometry and loading permits modelling of only one-quarter of the specimen. The mesh employs a hyperbolic mapping of the nodal coordinates yielding the crack plane mesh shown in Fig. 8(c). The total thickness of the cell layer in the crack opening direction represents the essential dimension within the computational cell methodology, therefore the cell dimensions in planes perpendicular to the initial crack front are fixed at $D/2 \times D/2$. Mesh refinement along the crack front direction needs only to capture the gradients of the fields. Twenty-eight (28) cell elements are defined along the half-crack front, where the dimension of the element along the crack front direction is D for elements close to the free surface and gradually increased to $8D$ for elements close to the symmetry plane of the crack front. Forty cell elements were used in the direction of crack extension so that a total of 1120 cell elements were utilized in the model. The total number of three-dimensional elements (eight nodes each) is 13 435 for SCT-1, 13 793 for SCT-2, and 13 600 for SCT-4 and SCT-6.

Symmetry boundary conditions are imposed over the

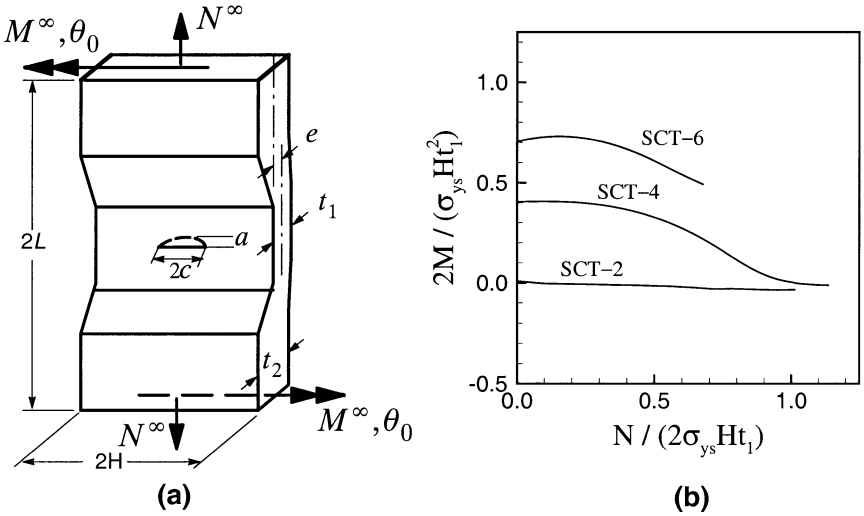

Fig. 7 (a) The geometry of a SCT specimen subject to combined tension and bending. (b) The M–N diagram taken from Faleskog[25] showing the loading histories of specimens SCT-1,2,4,6. N is the membrane force and M is the bending moment on the cracked section.

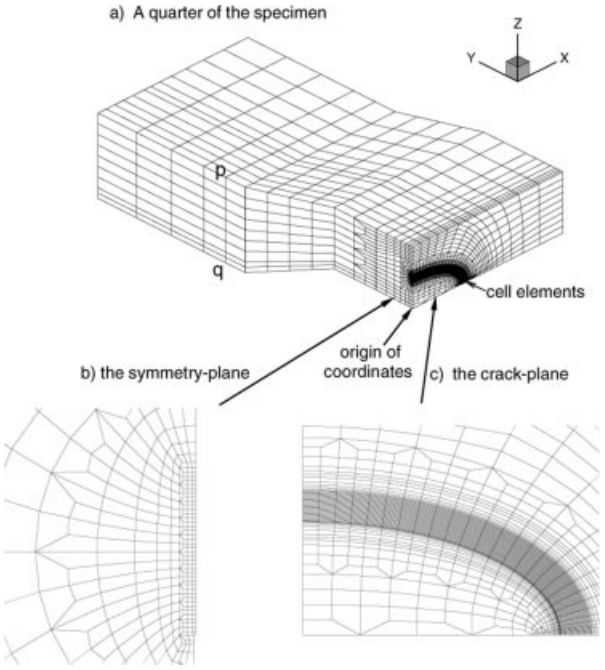

Fig. 8 Computational model of a slightly curved thick plate containing a part-through semi-elliptical crack displaying cell elements. (a) finite element mesh of a quarter of the plate. (b) Close-up of the *YZ*-plane of symmetry. (c) Close-up of the *XZ*-plane of the crack.

$X=0$ plane and $Y=0$ plane indicated in Fig. 8(a). Models for specimens SCT-2, 4 and 6 are loaded by imposing displacements over the remote end according to

$$u = w = 0$$
$$v = \delta - (Z - t_2/2)\tan\theta_0 \simeq \delta - (Z - t_2/2)\theta_0 \quad (5)$$

where *X*–Y–*Z* denotes the global coordinate system as shown in Fig. 8(a). These conditions model closely the clamped and rigidly moving boundary plane imposed in the experimental apparatus.

Specimen SCT-1 is loaded in three-point bending with a span of 450 mm between support rollers. Loading of the model takes place by imposing $w=0$ on nodes along the line $Z=0$, $Y=225$ mm and imposing $\Delta w<0$ displacement increments on top surface nodes along $Z=50$ mm, $Y<2$ mm.

Prediction of cleavage fracture

In this section, we employ the 'history approach' and apply the calibrated Weibull parameters to predict cleavage fracture in the surface-cracked specimens. As we mentioned in Section 4.2, the initial porosity (f_0) for the three-dimensional model is 0.0035, which is slightly smaller than the value for the plane strain model ($f_0=0.0045$). See Gao *et al.*[5] for a discussion of the difference in f_0 for the three-dimensional model and the plane strain model. Previous studies[3,15] suggest that ductile tearing elevates the stress triaxiality ahead of the crack tip, and thus increases the maximum principal stress and size of the high-stress zone. Our numerical calculations support this result, showing that a larger value of f_0, which results in a greater amount of ductile tearing at a certain level of J, leads to a higher failure probability by cleavage fracture at the loading stage when ductile tearing starts playing a role. However, our numerical results also show that the effect of the small difference of the two f_0 values used in this study on predictions of cleavage probability is insignificant for all crack geometries considered.

Figure 9 compares the predicted load–displacement responses with the experimental records for specimens SCT-1 [Fig. 9(a)] and SCT-4 [Fig. 9(b)]. For SCT-1, Δ_{LLD} represents the load-line displacement. For SCT-4, the axial displacements (v) are measured at two locations (p and q) remote from the crack plane on the symmetry plane of the specimen ($X=0$) at $Y=190$ mm. The plotted values of these displacements, δ_p and δ_q, represent the total elongation measured over a 380 mm gauge in the *Y*-direction (using the mirror image points for p and q at $Y=-190$ mm). The numerical model accurately captures the load–deformation history of both specimens. Similar comparisons were obtained for SCT-2 and SCT-6.

The solid curves in Fig. 10(a,b) display the predicted cleavage probability versus crack mouth opening displacement (CMOD) using the calibrated Weibull parameters from Section 4.3; (a) $\sigma_{th}=0$, $m=11.08$, $\sigma_u=11.86\sigma_0$ and (b) $\sigma_{th}=4$, $m=1.95$, $\sigma_u=109.24\sigma_0$. CMOD is used as a measurement of global loading for the different specimens and it is computed as the displacement between two points on the mid-plane of the surface crack each symmetrically located a distance 2.4 mm from the crack plane. The symbols in the figures pertain to the experimentally measured CMOD where cleavage fracture actually occurred in the tests. All fracture points lie within a probability band of $0.3 \leqslant P_f \leqslant 0.7$. Furthermore, specimens which were subjected to a higher degree of bending load (SCT-1,6) exhibit a more rapid development of cleavage failure probability with respect to CMOD than the more tension dominated tests (SCT-2,4), which reflects the influence of differences in constraint. Also, note that specimen SCT-4 experienced a greater bending load than specimen SCT-2, but SCT-2 has a slightly longer crack front, and as a result of both constraint and volume sampling effects, these two specimens show very close development of cumulative cleavage probabilities.

Note from equation (2) that the cleavage probability

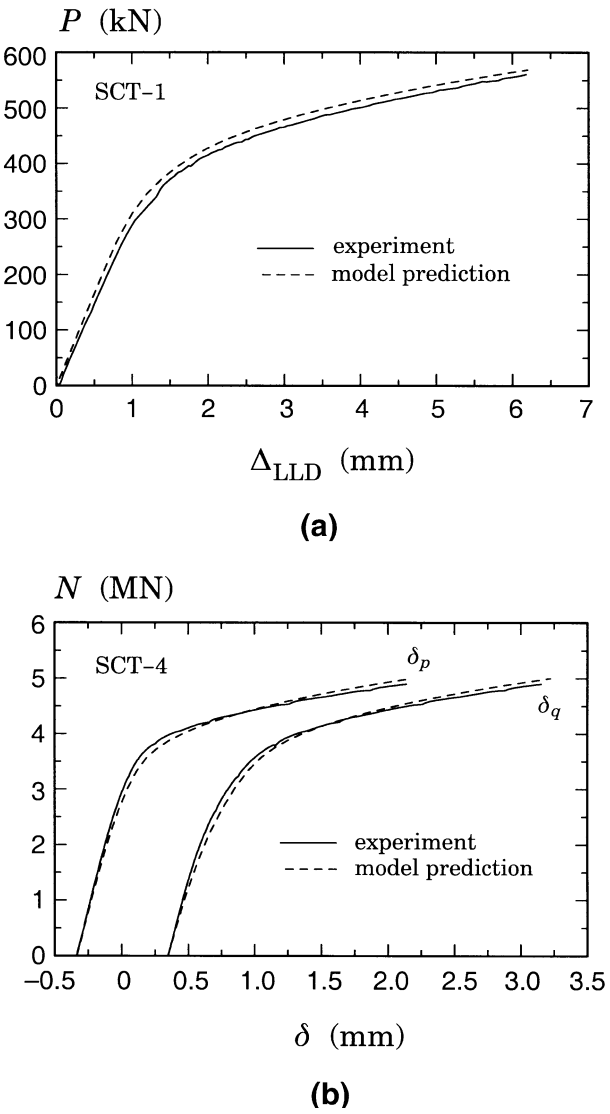

Fig. 9 Comparison of experimentally measured load versus displacement records with model predictions. (a) Specimen SCT-1 loaded in three-point bending, P and Δ_{LLD} are load and load-line displacement, respectively. (b) Specimen SCT-4 loaded in combined tension and bending, N is applied tensile force, and p and q refer to the positions where displacement data (δ) are measured.

is determined by the quantity $(\sigma_w/\sigma_u)^m$. In general, the contribution to this quantity is not uniformly distributed along the crack front direction. A new parameter ψ, which is defined as $(\sigma_w/\sigma_u)^m$ per unit length in the tangential direction of the crack front, measures this distribution, and the location where ψ is maximum indicates the most risky spot to find an 'eligible' particle to initiate cleavage fracture.

$$\psi_k = \sum_{i=1}^{n_k} \left(\frac{\sigma_1^i - \sigma_{th}}{\sigma_u} \right)^m \frac{V_i}{l_k V_0} \quad \text{for } V_i \tag{6}$$

where $\sigma_1^i \geqslant \sigma_{th}$ and $\bar{\varepsilon} > 0$

Here the half crack front in Fig. 8 is divided into 14 segments, and the elements close to the crack plane are arranged in 14 layers. l_k is the length of the kth segment, n_k is the total number of elements in the kth layer and V_i is the volume of the ith element in layer k.

Figure 10(c) and (d) displays the variation of ψ along the crack front, s, at the load level when cleavage fracture took place. Here, s is a normalized crack front coordinate, which is equal to zero at the deepest point of the initial crack front and equal to one at the free surface. The symbols in the plots indicate the actual cleavage initiation spots observed on the fracture surfaces. For specimens SCT-1, SCT-2 and SCT-4, the cleavage initiation spots very much coincide with the locations where ψ reaches its maximum. This is most clearly seen for SCT-1. The cleavage initiation spot of SCT-6 is very close to the location of maximum ψ. Faleskog[25] performed analysis using the toughness scaling model by Anderson and Dodds,[26] and obtained the same predictions of cleavage initiation location as the results presented in Fig. 10(c) and (d).

CONCLUDING REMARKS

In this study, we incorporate the cell model for ductile tearing with the weakest link statistics for cleavage fracture to analyse ductile/cleavage transition in a ferritic steel. The model takes into account the constraint effects, and puts no restriction on the extent of plastic deformation or amount of ductile tearing preceding cleavage failure. It is important to note that in this numerical approach all the statistical analysis can be performed as a post-processing step of the analysis. Therefore, the crucial part is accurately modelling ductile tearing and its effects on the stress and deformation fields. The cell model with a two-step model-calibration scheme (micromechanics calibration and fracture process calibration) has shown lots of success in different crack geometries and loading conditions for a wide range of structure steels.[5–8]

The statistical model is calibrated using experimental data containing a sufficiently large number of tests such that the model captures the scatter of cleavage fracture toughness. It is found that an increase in threshold stress (σ_{th}) results in a decrease in the calibrated Weibull shape factor (m) and an increase in the calibrated scaling stress (σ_u). Further study is needed to investigate the physical meaning of the threshold stress and determine its magnitude. However, our results show that the effect of threshold stress on prediction of cleavage fracture is insignificant for the material considered in this paper. The issue of two approaches to compute Weibull stress, the 'history approach' and the 'current approach', is also addressed in this paper.

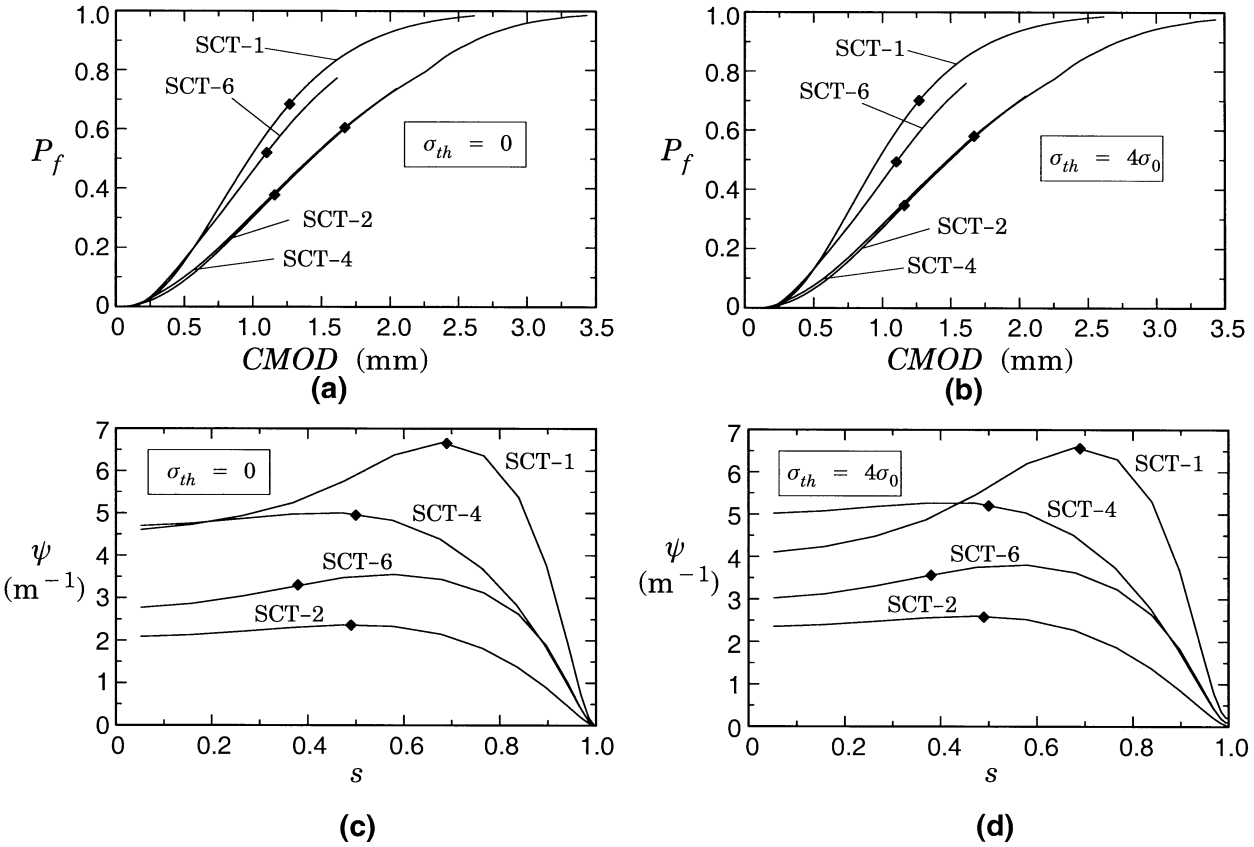

Fig. 10 (a), (b) Predicted cleavage probabilities for four SCT specimens. The symbols indicate values at which cleavage fracture actually occurred. (c), (d) Distribution of ψ along the crack front direction. s is the normalized distance along the initial crack front, which equals zero at the deepest point and one at the free surface. For (a) and (c), $\sigma_{th} = 0$; for (b) and (d), $\sigma_{th} = 4\sigma_0$.

The numerical model is finally applied to surface-cracked thick plates subject to different histories of bending and tension. The model accurately reproduced the load–displacement records and captured the constraint effect on cleavage failure probability. The SCT specimens subjected to a more pronounced bending load are exposed to a higher risk to fracture by cleavage at a given CMOD. A parameter ψ is defined as the distribution of $(\sigma_w/\sigma_u)^m$ along the crack front direction, and close agreement is revealed between the location of the cleavage initiation site on the crack front and the location where ψ reaches a maximum.

In this study, the experimental data used to calibrate the statistical model were obtained from a side-grooved specimen. However, side-grooves introduce several difficulties in the modelling. For example, side-groove effects on fracture process have not been extensively studied, and modelling side-grooves to adequately capture the highly local, non-uniform field requires lots of additional efforts. Due to these difficulties, the parameters in the Weibull model are calibrated using the plane strain model in this paper. The full three-dimensional calibration of this specimen type needs further investigation.

Acknowledgements

This investigation is supported by the Nuclear Regulatory Commission through Grant N61533-93-K-0030 from David Taylor Research and Development Center, and in part by the MRSEC Program of the National Science Foundation under Award Number DMR-9632524. X.G. is grateful to the Department of Solid Mechanics, Royal Institute of Technology (Sweden) for inviting him as a travelling scholar and providing him with the scholarship. Helpful discussions with professors F. Nilsson, K. Wallin and R. H. Dodds are also acknowledged.

REFERENCES

1 L. Xia and C. F. Shih (1995) Ductile crack growth—I. A numerical study using computational cells with microstructurally-based length scales. *J. Mech. Phys. Solids* **43,** 233–259.

2 L. Xia and C. F. Shih (1995) Ductile crack growth—II. Void nucleation and geometry effects on macroscopic fracture behavior. *J. Mech. Phys. Solids* **43,** 1953–1981.
3 L. Xia and C. F. Shih (1996) Ductile crack growth—III. Transition to cleavage fracture incorporating statistics. *J. Mech. Phys. Solids* **44,** 603–639.
4 J. Faleskog, X. Gao and C. F. Shih (1998) Cell model for nonlinear fracture analysis—I. Micromechanics calibration. Accepted for publication in *Int. J. Fracture* **89,** 355–373.
5 X. Gao, J. Faleskog and C. F. Shih (1998) Cell model for nonlinear fracture analysis—II. Fracture-process calibration and verification. Accepted for publication in *Int. J. of Fracture* **89,** 375–398.
6 L. Xia, C. F. Shih and J. W. Hutchinson (1995) A computational approach to ductile crack growth under large scale yielding conditions. *J. Mech. Phys. Solids* **43,** 389–413.
7 C. Ruggieri, T. L. Panontin and R. H. Dodds (1997) Numerical modeling of ductile crack growth in 3D using computational cell elements. *Int. J. Num. Meth. Engng* **82,** 67–95.
8 X. Gao, J. Faleskog, R. H. Dodds and C. F. Shih (1998) Ductile tearing in part-through cracks: Experiments and cell-model prediction. *Engng Fracture Mech.* **59,** 761–777.
9 A. L. Gurson (1977) Continuum theory of ductile rupture by void nucleation and growth: Part I—yield criteria and flow rules for porous ductile media. *J. Engng Mater. Tech.* **99,** 2–15.
10 V. Tvergaard (1981) Influence of voids on shear band instabilities under plane strain conditions. *Int. J. Fracture* **17,** 389–407.
11 V. Tvergaard (1982) On localization in ductile materials containing spherical voids. *Int. J. Fracture* **18,** 237–252.
12 C. J. McMahon, Jr and M. Cohen (1965) Initiation of cleavage in polycrystalline iron. *Acta Metall.* **13,** 591–604.
13 Y. Y. Wang (1991) A two-parameter characterization of elastic–plastic crack-tip and applications to cleavage fracture. PhD thesis, Department of Mechanical Engineering, MIT.
14 G. T. Hahn (1984) The influence of microstructure on brittle fracture toughness. *Metall. Trans. A* **15A,** 947–959.
15 C. Ruggieri and R. H. Dodds, Jr (1996) A transferability model for brittle fracture including constraint and ductile tearing effect: a probabilistic approach. *Int. J. Fracture* **79,** 309–340.
16 X. Gao, C. F. Shih, V. Tvergaard and A. Needleman (1996) Constraint effects on the ductile-brittle transition in small scale yielding. *J. Mech. Phys. Solids* **44,** 1255–1282.
17 D. A. Curry and J. F. Knott (1979) Effect of microstructure on cleavage fracture toughness of quenched and tempered steels. *Mater. Sci.* **13,** 341–345.
18 F. M. Beremin (1983) A local criterion for cleavage fracture of a nuclear pressure vessel steel. *Metall. Trans. A* **14A,** 2277–2287.
19 F. Mudry (1987) A local approach to cleavage fracture. *Nuclear Engng Design* **105,** 65–76.
20 A. Bakker and R. W. J. Koers (1991) Prediction of cleavage fracture events in the brittle-to-ductile transition region of a ferritic steel. In: *Defect Assessment in Components—Fundamentals and Applications* (Edited by J. G. Blauel and K.-H. Schwalbe), ESIS/EGF9. Mechanical Engineering Publications, London, pp. 613–632.
21 K. Wallin (1993) Statistical aspects of constraint with emphasis on testing and analysis of laboratory specimens in the transition region. In: *Constraint Effects in Fracture*, *ASTM STP 1171* (Edited by E. M. Hackett, K.-H. Schwalbe and R. H. Dodds), American Society for Testing and Materials, Philadelphia, pp. 265–288.
22 R. W. J. Koers, A. H. M. Krom and A. Bakker (1995) Prediction of cleavage fracture in the brittle to ductile transition region of a ferritic steel. In: *Constraint Effects in Fracture*, *Theory and Applications*, *ASTM STP 1244* (Edited by M. Kirk and A. Bakker), American Society for Testing and Materials, Philadelphia, pp. 191–208.
23 R. Van Stone, T. Cox, J. Low and J. Psioda (1985) Microstructural aspects of fracture by dimpled rupture. *Int. Metals Rev.* **30,** 157–179.
24 F. Nilsson, J. Faleskog, K. Zaremba and H. Oberg (1992) Elastic–plastic fracture mechanics for pressure vessel design. *Fatigue Fract. Engng Mater. Struct.* **15,** 73–89.
25 J. Faleskog (1995) Effects of local constraint along three-dimensional crack fronts—a numerical and experimental investigation. *J. Mech. Phys. Solids* **43,** 447–493.
26 T. L. Anderson and R. H. Dodds, Jr (1991) Specimen size requirements for fracture toughness testing in the ductile-brittle transition region. *J. Testing and Evaluation* **19,** 123–134.